FUNDAMENTALS & APPLICATIONS

CHEMELECTROCHEM

ANALYSIS & CATALYSIS, BIO & NANO, ENERGY & MORE

# Accepted Article

**Title:** Electrodeposition of sea-urchin and cauliflower-like Ni/Co doped manganese dioxide hierarchical nanostructures with improved energy storage behavior

**Authors:** Manickam Minakshi; Avijit Biswal; Bankim Tripathy



**To be cited as:** ChemElectroChem 10.1002/celc.201600071

**Link to VoR:** http://dx.doi.org/10.1002/celc.201600071

A Journal of

ChemPubSoc Europe

www.chemelectrochem.org

WILEY-VCH

# Electrodeposition of sea-urchin and cauliflower-like Ni/Co doped manganese dioxide hierarchical nanostructures with improved energy storage behavior

**[1]Avijit Biswal, [1]Manickam Minakshi*, and [2]Bankim Chandra Tripathy**

[1]School of Engineering and Information Technology, Murdoch University, Murdoch, WA 6150, Australia

[2]CSIR, Institute of Minerals and Materials Technology, Bhubaneswar 751013, India

## Abstract

Transforming the existing Zn-$MnO_2$ primary battery into a secondary battery resulting in enhanced storage behavior with low cost is of significant interest. Such technology could underpin future energy storage development. To acquire this, doped electrolytic manganese dioxide (EMD) with hierarchical nano architectures have been employed as a cathode in Zn-$MnO_2$ system. EMD is synthesized from manganese sulphate in sulphuric acid bath with in-situ doping of nickel and cobalt ions individually. Sea-urchin shaped EMD has been obtained for nickel as a dopant while cauliflower and pyramidal shaped hierarchical nanostructures are observed for cobalt as a dopant using a facile galvanostatic method without employing any template or surfactant. The structural studies indicated that all the EMD samples (in the absence and presence of dopants) predominantly composed of gamma-type manganese dioxide, however, peak intensity increased with the increase in concentration of the dopants. The electrochemical results revealed that Co doped EMD composite played a crucial role in increasing the storage capacity of the Zn-$MnO_2$ battery while Ni doped EMD composite resulted in improved longevity than the Co and undoped counterparts. The EMD doped with Ni and Co composites individually resulted in improved storage behavior of 395 and 670 mA h $g^{-1}$ respectively, against the undoped sample which is 220 mA h $g^{-1}$, implying the presence of $Co_3O_4$ and mesoporous nanostructured surface enhanced the fast kinetics of electrochemical reactions.

*E: minakshi@murdoch.edu.au

## 1. Introduction

In the current decade there has been a much emphasis on transition from conventional non-renewable fossil fuels towards the renewable energy sources, but due to the intermittent nature of the renewable sources (solar, wind etc.), excess renewable generation need to be stored for later use. Energy storage plays a vital role to reduce or avoid demand costs during peak periods specified by the network. In this context, batteries and electrochemical capacitors are the best candidates for the future energy crisis. The electrochemical storage of energy by means of rechargeable batteries shows a tremendous potential of growth. An aqueous rechargeable cell is an affordable and safe option to store power from renewable generation. Extensive research are underway to develop an ecofriendly, cost effective, earth abundant, novel energy material possessing high energy density and specific capacity with improved cycleability. Lithium-ion batteries using non-aqueous solutions are currently dominating the market. However, alkaline batteries for over three decades retain its importance in the field of consumer electronics devices such as low drainage power systems. This is due to the nature of cathode material such as electrolytic manganese dioxide (EMD) coupled with metallic Zn as anode in KOH electrolyte.

In the ever increasing demand of market for rechargeable batteries and electrochemical capacitors, transition metal oxide such as manganese, nickel, cobalt etc. as cathode have drawn much attention with their striking electrochemical properties [1-8] irrespective of their pros and cons. Recently, cobalt oxides ($Co_3O_4$ and CoO) have received much attention among the researchers as an anode material for lithium ion batteries due to its high theoretical capacity of 892 mA h $g^{-1}$ and abundant in nature [9-11], however, the major drawback of this material is of high cost. On the other hand, nickel oxide (NiO) with theoretical capacity of 718 mA h $g^{-1}$ is less expensive than CoO [12] has also drawn attention in rechargeable battery system due to its unique hollow structure [13]. Whereas, manganese dioxide ($MnO_2$) despite its

lower theoretical capacity of 308 mA h $g^{-1}$ has been in high demand for its use as a cathode material in primary as well as secondary batteries. This is due to the characteristic nature of manganese such as factors including environmentally benign, low cost, and abundant in nature [14-19] when compared to other metal oxide used for batteries such as nickel and cobalt-oxides. Nevertheless, the major setback of the $MnO_2$ material is the formation of Jahn-teller distortion that limits its reversibility. Continual attempts are underway in terms of alleviating this issue through adding suitable transition metal ions as dopants via both ex-situ and in-situ to maintain the structural stability and its reversibility. Attempts [20-26] have also been made to produce bivalent oxide/mixed oxide (i.e. manganese molybdenum, nickel manganese, cobalt manganese oxide etc.) cathode materials for better energy storage. Most of the reported electrodeposition methods for producing electrolytic manganese dioxide (EMD) are pertained to potentiostatic technique. Doping transition metal ions to the $MnO_2$ material via conventional synthetic routes [27-30] are quite common and widely researched area. However, the production of EMD having addition of transition metal ions as dopants via *in-situ*, and scaling up through facile galvanostatic electrodeposition method is not widely reported for battery applications. Therefore, we have proposed the facile galvanostatic electrodeposition approach here.

In the current work, we have examined the in-situ doping of transition metal ions such as nickel and cobalt in the bath containing manganese sulphate in sulphuric acid to electrodeposit EMD without employing any templates or surfactants. To the best of our knowledge, this sort of unique approach with the formation of hierarchical nanostructures has not been reported for alkaline battery applications. The $MnO_2$ was doped with nickel (or) cobalt to provide electronic stability to the $Mn^{3+}$ state that are believed to disproportionate to $Mn^{2+}$ and $Mn^{4+}$ states and mitigate the formation of Jahn-Teller distortion. The objective of this work is to synthesize the Ni and Co doped EMD separately and to understand the role of

dopants in energy storage behaviour. The synergistic effect of both the dopants CoNiEMD has also been studied and reported here in the electronic supporting information (ESI).

With these objectives in mind, the EMDs synthesized from pure manganese sulphate in sulphuric acid bath in the presence and absence of nickel sulphate (or/and) cobalt sulphate as dopants were electrochemically evaluated by charge-discharge, cyclic voltammetry and electrochemical impedance analyses for its suitability in alkaline battery applications. Our electrochemical studies indicate that the cauliflower and pyramidal like nanostructured Co doped EMD exhibit improved storage behavior compared to un-doped EMD as cathode material in rechargeable Zn-EMD cells. On the other hand, Ni doped EMD showed cycling stability with high capacity retention showing the best electrochemical activity. The obtained nanostructured particles have larger surface areas that enable fast diffusion rates resulting in enhanced storage and excellent capacity retention [31]. The hierarchical structured EMD as a cathode for rechargeable battery provide the large contact area between the electrode and electrolyte interface that lead to improve the cycle life of the $MnO_2$ and also the large capacity due to additional space for the electrolyte accommodation [32]. In the present study, Ni or Co doped EMD samples showed two hierarchical arrangements. A spherical shaped Co (or) Ni agglomerated particles is covered by spine shaped $MnO_2$ possessing a hierarchical structure with high surface area for easy transport of electrolyte. The performance characteristics and the role of dopants in energy storage are discussed. The proposed aqueous Zn-$MnO_2$ rechargeable battery offers immediate advantages over existing technologies (Pb-$PbO_2$, Ni-Cd, Ni-MH) with respect to cost, safety, and environmental considerations.

## 2. Experimental Section

### *2.1. Material synthesis*

All the chemicals used in this work were of analytical grade and used as received. Pure electrolytic manganese dioxide (EMD) was synthesized from a manganese sulfate in

sulphuric acid bath containing 3.36 mol $dm^{-3}$ manganese sulphate with 0.3 mol $dm^{-3}$ sulphuric acid at an anodic current density of 200 A $m^{-2}$ in a thermostatic glass cell. The detail of the experimental set-up has been outlined in our previous work [33]. Two different concentrations of nickel doped EMDs were deposited from baths containing (a) 2.51 mol $dm^{-3}$ Mn + 1.15 mol $dm^{-3}$ Ni with 0.22 mol $dm^{-3}$ sulphuric acid, and (b) 1.68 mol $dm^{-3}$ Mn + 2.28 mol $dm^{-3}$ Ni with 0.15 mol $dm^{-3}$ sulphuric acid. The samples electrodeposited with the above said concentrations were labelled as NiEMD1 and NiEMD2, respectively. Likewise, two different concentrations of cobalt doped EMDs were deposited from baths containing (a) 2.51 mol $dm^{-3}$ Mn + 1.21 mol $dm^{-3}$ Co with 0.22 mol $dm^{-3}$ sulphuric acid and (b) 1.68 mol $dm^{-3}$ Mn + 2.42 mol $dm^{-3}$ Co with 0.15 mol $dm^{-3}$ sulphuric acid. They were labelled as CoEMD1 and CoEMD2, respectively. The details of the electrolyte composition (g $dm^{-3}$) from which different EMDs were synthesized have been shown in Table 1. Apart from the above said compositions, the Ni or Co dopant concentration in the bath cannot be increased further. By doing so, the Mn concentration in the bath will reach below the threshold of 1.68 mol $dm^{-3}$ that resulted in a high energy consumption for EMD synthesis. Therefore, the dopant concentration has been limited to 2%.

During the electrodeposition, the inter-electrode gap of 3 cm between the stainless steel (SS) cathode and lead (Pb) anode had been maintained in a thermostatic glass cell set up. The electrode area exposed for electrodeposition was 6.5 cm * 5.8 cm. The laboratory scale experiments were carried out in stagnant solution in batch mode. All experiments were carried out at 90±5°C for 3 h. Constant current was given from a DC power supply (MANSON, 0-30V, 2.5A). The anodic oxidation of $Mn^{2+}$ to $MnO_2$ was carried out on a Pb anode placed in parallel to a stainless steel cathode. The electrodeposition is carried out through the following reactions, represented in Eqs. (1-2):

$$\text{At anode: } Mn^{2+} + 2H_2O \longrightarrow MnO_2 + 4H^+ + 2e^- \quad (1)$$

At cathode: $2H^+ + 2e^- \longrightarrow H_2$ (2)

The formation of EMD ($MnO_2$) takes place through intermediate products such as MnOOH and $Mn_2O_3$ in $Mn^{3+}$ form. In acidic sulphate bath, the $Mn^{3+}$ ion undergoes a disproportionate reaction forming $Mn^{4+}$ and $Mn^{2+}$ (soluble) ions. After deposition, the dried mass of EMD ($Mn^{4+}$) was ground and sieved through a 53-μm mesh to obtain EMD in a powder form. The resultant powder was then washed repeatedly with deionized water until the sample was sulphate free. The obtained product termed "EMD powder" was finally dried and cooled in a desiccator followed by its physical and electrochemical characterizations. To assess the lead contamination in the EMD powder, the elemental analysis has been carried out through atomic absorption spectrometer. The digested EMD sample confirmed that lead (Pb) content was found to be below the detection limit. Morphological characterization was performed on electrodeposited EMD scraped from the anodes followed by thorough washing with deionized water.

### *2.2. Physicochemical characterization*

X-ray diffraction (XRD) patterns were measured with Siemens D500 X-ray diffractometer 5635 using Cu Kα radiation (λ = 1.54 Å) at 35kV and 28 mA. The data were recorded from $10^o$ – $70^o$ with scan speed of 1° per min. Microstructures of the prepared samples, were investigated by a high magnification Tescan Mira3 focussed ion beam-scanning electron microscope (FIB-SEM) with an energy dispersive X-ray detector (EDS) (Oxford X-Max 150 SDD detector and AZtec software) for elemental analysis. The transmission electron microscopy (TEM) imaging were carried out using an electron microscope (FEI, TECNAI G2 20, TWIN) operating at 200 kV, equipped with a GATAN CCD camera. Samples were prepared by first mixing a small amount of the material with ethanol, sonicating the suspension and then placing a single drop of the resulting suspension onto a 200 mesh carbon-coated copper grid, which was then allowed to dry in air. Selected area electron diffraction (SAED) patterns were

obtained with the smallest area aperture available (10 mm). Brunauer, Emmett and Tellet (BET) surface area measurement and porosity analysis were carried out by Micromeritics Tristar II Surface area and porosity analyser. Before analysing, the samples were degassed at 100 °C overnight. Inductive coupled plasma (ICP) technique was employed for the elemental analysis of the doped EMD materials. The quantitative amount of Ni and Co present in the electrodeposited EMD are calculated to be 1 % and 2% respectively for NiEMD1 and CoEMD2 respectively.

### *2.3. Electrochemical characterization*

Charge-discharge measurements were carried out in a two electrode system by using a battery tester. The electrochemical "flooded cell" comprised of EMD cathode and Zinc anode immersed in potassium hydroxide (9M) solution as the aqueous electrolyte. The cathode consisted of an active material made of undoped or doped EMD (75wt %), acetylene black (AB, 15wt %) and poly vinylidene fluoride (PVDF, 10 wt. %) mixed uniformly in an agate mortar in the presence of 0.3-0.4 mL of N-methyl-2-pyrrolidinone (NMP). The slurry was then coated on a graphite sheet of 1 $cm^2$ and dried at 60 °C for an hour. The weight of the active material was calculated from the weight of the graphite electrode before and after coating. The coated electrode was then masked with a non-conducting tape (except the coated sample analysis area). A metallic zinc strip was used as the anode with a mass of at least two times to that of the cathode. The applied current density for these experiments was 2 mA $cm^{-2}$ with discharging and charging cut-off voltages of 0.9 and 1.75 V respectively. Cyclic voltammetry (CV) and electrochemical impedance spectroscopy (EIS) studies were carried out in a three electrode system using a BioLogic VSP-300 instrument. The working electrode used in this system was EMD and metallic Zn strip as the counter electrode. Mercury–mercuric oxide (Hg/HgO) served as the reference electrode with 9M KOH as the electrolyte. During CV studies the material was cycled in the potential window of 0.2 V to -0.6 V in

cathodic direction initially and then reversed the scan with a constant scan rate of 0.15 $mVs^{-1}$. Impedance of the Zn-EMD cell was recorded in the frequency range between 100 kHz and 1 mHz with amplitude of 10 mV.

.

## 3. Results and discussion

### *3.1 Physicochemical characterization*

The X-ray diffraction (XRD) patterns of the undoped and doped EMD samples are shown in Figure 1. The undoped EMD sample in Fig. 1a showed a diffraction pattern having five major peaks at various 2θ values such as $22^o$ (110), $37.2^o$ (021), $42^o$ (121), $56^o$ (240/221) and $68^o$ (002/061) without any second phase as an impurity indicating the electrodeposited product is pure-phase $MnO_2$. These diffraction peaks can be indexed to an orthorhombic phase of γ-type $MnO_2$ with lattice constants: $a$ = 8.70 Å, $b$ = 2.90 Å and $c$ = 4.41 Å. These cell parameters are in good agreement with the standard values of JCPDS card no. 65–1298 ($a$ = 9.27 Å, $b$ = 2.87 Å, $c$ = 4.53 Å). However, when comparing the diffraction pattern obtained for undoped EMD with the doped EMD in Fig. 1 b-e, undoped material shows poor crystalline in nature than the doped material, while the intensity of the peaks increases with an increase in the concentration of the transition metal ions in the bath. This indicates the order of crystallinity increases in the presence of dopants. The diffraction peaks for the synthesized Co doped material (Fig. 1 d-e) showed minor peaks corresponding to $Co_3O_4$ and CoO as impure phases [34].With the higher concentration of cobalt in the bath, the extent of the formation of $Co_3O_4$ appears to be intense illustrating the Co has been included in the electrodeposited EMD in the form of $Co_3O_4$ and CoO oxides. Additionally, a minor peak at $27^o$ is also seen for all the EMD samples which cannot be attributed to any known manganese, cobalt or nickel phases provided in the database.

Figure 2(a) and (b) showed the nitrogen adsorption-desorption isotherms and the corresponding Barrett–Joyner–Halenda (BJH) pore-size distribution curves of EMD (undoped), NiEMD2, and CoEMD2 respectively. The adsorption and desorption behaviour observed for all the samples corresponds to the type IV isotherm with a H2 type hysteresis loop confirming the mesoporosity. Doped samples such as NiEMD2, CoEMD2 showed a loop shifting to a higher relative pressure approaching $P/P_0 = 0.98$ suggesting large number of mesopores are present comparing to that of the undoped EMD. The extent of mesoporosity appears to be higher for CoEMD2 followed by NiEMD2 sample. BJH pore size distribution curve showed a significant difference between the undoped and the doped EMD samples. EMD (undoped) showed a narrow pore size distribution curve centred at about 4 nm, however broadening in pore size distribution curve were observed for the doped samples (NiEMD2, CoEMD2) which centred at about 6-7 nm (Fig 2b) suggesting larger pore size, with an easy transfer of electrolyte through the doped EMD making the electrode versatile for accommodating host ions. The surface areas of the as-prepared EMD, NiEMD2, CoEMD2 were found to be 91, 108, and 130 $m^2 g^{-1}$ respectively.

Surface morphologies of the undoped and doped EMDs were examined through FIB-SEM and TEM and the results are shown in Figs. 3 – 5 and Fig. S1 (ESI). As observed from the images, undoped EMD in Fig. 3a1 exhibits homogenous long needle shaped $MnO_2$ particles with a length of about 100 nm, oriented in net like fashion having compact morphology. The corresponding TEM imaging (in Fig. 5a) shows rice-grain shaped coarse particles of 80 – 100 nm. At a higher magnification, a needle shaped unevenly distributed particles with varying sizes are clearly seen in Fig. 5 a1. On introduction of nickel (0.5%) in the bath, Fig. 3b, the surface morphology of the electrodeposited EMD changed dramatically leading to the formation of smaller sphere like aggregate (1- 2 μm in diameter) corresponding to the nickel dopant covered with needle shaped $MnO_2$ particles. At a higher magnification,

thick thorn shaped grains oriented perpendicular towards the plane, is seen in Fig. 3 b1. However, while increasing the nickel concentration from 0.5% to 1%, NiEMD2 showed distinctive spheres (Fig. 3 c) comprised of nano needle like thorns oriented in orderly pattern (Fig. 3 c1) termed as sea-urchin like hierarchical nanostructures. The image in Fig. 3 c1 shows typical two hierarchical nanostructured pattern with spherical NiO wrapped with $MnO_2$ thorns. It can be inferred that the rate of formation of nuclei on the substrate was higher and that the amount of deposits increased substantially for the higher concentration of nickel (NiEMD2). A typical transmission electron microscopy (TEM) imaging (Fig. 5b) of NiEMD2 powder after grinding confirms the presence of nano needle like thorns observed previously (in Fig. 3c1). It consists of cluster of uneven thorns with length ranging between 30 – 50 nm. The high resolution TEM (Fig. 5 b1) and the corresponding selected area electron diffraction pattern (SAEDP in Fig. 5 b2) showed that the well-defined $MnO_2$ thorns were uniformly covered on NiO particles. These particles are crystalline in nature having series of rings with bright diffraction spots in it. Hence, the observed sea urchin like morphology is a nanostructured crystalline in nature. In a separate experiment, on introduction of cobalt (1%) in the bath, it is interesting to note that cauliflower growths of the CoEMD1 crystallites were observed in Fig. 4a. However on magnifying the image, it was observed that, each cauliflower like crystallite composed of nano flower buds shaped grains (in Fig. 4 a1) within the range of 50-100 nm. The bulk cauliflower shaped particle corresponds to $Co_3O_4$ particles while the surface nano flower buds correspond to $MnO_2$ particles. The cross-sectional view of this sample at different locations showed a uniform flower bud shaped nano grains (in Fig. 4 b & b1) ascertaining the formation of hierarchical Co/Mn nanostructures through the facile electrodeposition route [35-36]. While varying the concentration of Co (from 1 % to 2 %) in the bath, CoEMD2 sample, again quite a different morphology was observed. The image in Fig. S1 a showed array of pyramid like crystallites

oriented uniformly leaving behind pores across them. At a higher magnification, it was observed that each pyramid composed of star shaped nano grains within the range of 100 nm (Fig. S1 a1). The nanostructure pyramidal alignment shown in Fig. S1 a1, radiates from the centre of the crystal forming the star shaped deposition. The deposition of EMD with Co dopants resulted in a homogenous deposit, but the length of the rods (< 20 nm) as evidenced from TEM imaging (compare Fig. 5 b1 and c1) was significantly smaller than the NiEMD2 illustrating the difference seen is attributed to the high adsorption of cations. The hierarchical nanostructures can provide the synergistic effect of the individual cations in the $MnO_2$ composite cathode. The evidence of porous nature of CoEMD2 was confirmed from both porosity analysis and morphology studies. The energy dispersive analysis (EDS) data shown in Fig. S2 confirmed the presence of pure Mn and O peaks for EMD sample. However, evolutions of Ni and Co peaks were observed for NiEMD and CoEMD samples with a very low intensity suggesting the presence of Ni and Co as composites in a very low quantity in EMD structure. This was supported quantitatively by the ICP analysis.

**3.2 Electrochemical characterization**

The electrodeposited sea-urchin and cauliflower/pyramidal shaped EMD hierarchical structures appear to be an ideal cathode material for Zn-EMD cells. As a comparison, undoped EMD needle shaped particles as cathode has also been electrochemically tested under the same conditions. Higher current density (200 A $m^{-2}$) applied during the electrodeposition generate higher rate of nucleation and anode potential [35-37]. These factors resulted in larger surface area with a porous nature, as discussed in the earlier section 3.1. For the chosen bivalent $Ni^{2+}$ or $Co^{2+}$ dopants, the effect of nucleation rate promotes the adsorption of these ions due to their activity for adsorption [38]. Taken the above together, the doped EMD have been successfully electrodeposited with improved physicochemical

characteristics of smaller particle size that enable for their use as electrodes in rechargeable alkaline batteries.

Both galvanostatic (charge/discharge) as well as potentiostatic (cyclic voltammetry) studies in assistance with electrochemical spectroscopy (EIS) were carried out to evaluate the electrochemical activity of the EMD samples for its plausible application in aqueous rechargeable battery. In the aqueous (KOH) battery, the oxidation occurs at the zinc anode and the reduction occurs at the EMD cathode. For the charge-discharge studies, the EMD electrodes were subjected to discharge followed by charge under identical conditions in 9M potassium hydroxide solution. The typical discharge-charge profiles for undoped and doped EMD (NiEMD2 and CoEMD2) samples were compared in Fig. 6, which revealed that a constant flat voltage profile is observed for all the samples in the voltage region of about 1.2 V. The extent of discharge plateau has been found longer for the Co doped EMD sample. The NiEMD2 cell exhibited a discharge capacity of 395 mA h $g^{-1}$ while CoEMD2 exhibited a higher discharge capacity of 670 mA h $g^{-1}$ against the undoped sample which is of only 220 mA h $g^{-1}$. The influence of Ni and Co as dopant showed improved discharge behaviour but irrespective of the dopants in the EMD cathode all the cells are found to be reversible at higher current rates illustrating that they are suitable for high power applications.

The redox processes of undoped EMD during charge-discharge are quite similar to that has been discussed in one of our previous works [33]. In the case of doped EMD, in addition to the potassium intercalation reaction mechanism, the following possible additional conversion reactions (Eqs. 3-5) also can undergo during the electrochemical process for the samples NiEMDs and CoEMDs respectively [39 - 40].

$$NiO + OH^- \Leftrightarrow NiOOH + e^- \quad (3)$$

$$Co_3O_4 + OH^- + H_2O \Leftrightarrow 3CoOOH + e^- \quad (4)$$

$$CoO + OH^- + \Leftrightarrow CoOOH + e^- \quad (5)$$

Figure 7 shows the comparison of discharge capacity vs. cycle number for the undoped and doped EMD material. The undoped EMD showed an initial discharge capacity of 220 mA h $g^{-1}$, however on addition of dopants the initial discharge capacity of EMD increases beyond its theoretical capacity of 308 mA h $g^{-1}$. The presence of 0.5% nickel (NiEMD1) in EMD composite enhanced its discharge capacity to a value of 285 mA h $g^{-1}$, on increasing the doping amount up to 1% (NiEMD2) capacity is further increased to a higher value of 395 mA h $g^{-1}$. The observed excess capacity could be due to a formation of NiOOH which is electrochemically reversible [41]. In the case of Co doped EMD with 1% dopant (CoEMD1) resulted in a high initial discharge capacity of 268 mA h $g^{-1}$, with an increase to 2 % dopant (CoEMD2), a maximum amount of 670 mA h $g^{-1}$ has been achieved. The observed charge-discharge trend showed an interesting assumption that, the obtained discharge capacity of the doped EMDs was not proportionate to the amount of doping. The increase in discharge capacity from NiEMD1 to NiEMD2 in proportion with percentage of doping from 0.5 to 1% respectively was quite lower than the case obtained for Co as dopant. This trend could be explained from the difference seen in morphology and crystal structure of the electrodeposited material. The observed high capacity for CoEMD2 is attributed to the formation of CoOOH which is less reversible in the successive cycles. The large surface area of CoEMD2 with 130 $m^2$ $g^{-1}$ that possess porous pyramid shaped morphology having CoO and $Co_3O_4$ in the composite may increase the utilization of this material and thus the observed high capacity (670 mA h $g^{-1}$). [9] Also, the presence of larger number of mesopores with large pore size is in favour of improving the electrochemical accessibility of ions from the KOH electrolyte and providing preferable pathway for reversible intercalation [41]. A significant difference observed from Figure 7 (inset) is the poor cycleability and the available capacity noted for undoped EMD. The capacity fade on cycling suggests the undoped $MnO_2$ underwent active material loss in strong alkaline solution resulting from the dissolution of

$Mn^{2+}$ ions. On the other hand, the Ni doped EMD (NiEMD1) showed the best cycle life stability followed by NiEMD2. The stable cyclic behaviour could be due to the structural stability of the $MnO_2$, mitigating the Jahn-Teller distortion, arising from the presence of nickel in the EMD composite. The sharp decline in capacity after the fifth cycle (shown in the inset) for all the samples could be due to irreversible behaviour of proton/potassium-ion intercalation into the host $MnO_2$ lattice. Overall, the observed fall in discharge capacity retention is a typical characteristic of Zn-$MnO_2$ battery in aqueous electrolyte [42-44]. The available capacity after multiple cycles (65 mA h $g^{-1}$) and the energy storage retention are found to be high for the NiEMD1 sample in the alkaline system. The performance characteristics of the EMD doped composites in the Zn-$MnO_2$ battery system (shown in Figs 6 & 7) outperformed the existing alkaline technology reported in the literature [42-44]. The transition metal ions in the electrolytic bath strongly affect the nucleation and growth of EMD resulting in highly porous sea-urchin and flower shaped nano architecture that supports faster ionic transport through the EMD structure that resulted in enhanced discharge capacity and reversibility.

Cyclic voltametric (CV) studies were carried to demonstrate the redox behaviour of the synthesized EMD samples. Figure 8 shows the current vs. voltage profiles for the undoped and doped EMD samples. In each case, scan was initiated at 0.2 V vs. Hg/HgO in the cathodic direction to -0.6 V at a scan rate of 0.15 mV $s^{-1}$. The results revealed that undoped EMD showed a reduction peak C1 at about -0.3 V due to the reduction of $MnO_2$ species with the corresponding oxidation peak A1 at -0.01 V. The reduction and oxidation maxima are due to the redox species $Mn^{+4}/Mn^{+3}$ for all the EMD samples, however, doped EMDs (both NiEMD and CoEMD) showed an additional reduction peak C2 indicating the dopant cations participate in conversion reactions as stated in Eqs. (3-5). The prominent C2 peaks for Ni and Co dopants illustrate both the faradaic and non-faradic reactions occurred while the C1 peaks

are predominantly due to intercalation (faradaic) reactions. NiEMD1 showed reduction peaks at -0.09 V (C2) and -0.27 V (C1) corresponding to the reduction of nickel [45-47] and manganese[48] species respectively. NiEMD2 showed C2 and C1 at -0.10V and -0.28 V respectively. NiEMD sample exhibited higher redox current than that of the undoped EMD indicating the utilization of the active material is high in the presence of dopants. The mesoporous sea-urchin nanostructure morphology was contributed to the improved performance of NiEMD sample. CoEMD2 showed reduction peaks at -0.11V (C2), -0.32 (C1) corresponding to the reduction of cobalt (C2) [49-51] and manganese[48] species (C1) respectively. The area under the curve for CoEMD2 is much higher than the NiEMD and EMD, showing a structural stability and strong reduction mechanism occurs for manganese in presence of cobalt indicating better faradaic behaviour. This is due to the highly porous nanostructured morphology with a larger pore size for the CoEMD2 sample as evidenced from nitrogen adsorption-desorption and FIBSEM images. The well-defined redox peak indicates fast charge transfer due to highly accessible pore structure suggesting rapid and unhindered diffusion of ions[52] as a result of which the sample showed highest initial discharge capacity than the Ni doped and undoped EMD samples. Another important observation from the CV curves to be noted is that the doped EMD samples showed minimum peak separation (0.27 V) than the undoped one which is 0.3 V indicating the material showing better reversibility[48, 53-54] and the enhanced area under the peak denotes the improved energy storage for the doped samples.

The performance and reversibility of a material strongly depends upon its unique morphology and porosity [49-51]. Among the materials investigated, the improved storage capacity observed for CoEMD2 could be attributed due to one or all of the following (a) nanostructured grain size (50 – 100 nm) which shortens the diffusion path length, (b) the highly ordered mesoporous nature (Fig. 2) supported by the γ-$MnO_2$ phase (Fig. 1)

possessing tunnel structure that facilitates easy ionic diffusion thereby increasing the active sites for intercalation mechanism to occur, and (c) the star shaped nano architecture (Fig. S1) having pyramidal alignment create an open space in between them which aids the easy diffusion of electrolyte into doped EMD resulting in maximum utilisation of the active material.

Although improved storage behaviour has been achieved for CoEMD2 among the samples studied, to further enhance the storage capability, it is thus of great interest to the rational composition and fabrication of CoNiEMD based electrode. The electrochemical results for this sample is detailed in the Figs S3 – S5 in ESI and found that it is not suitable for a battery system.

The optimised dopant concentration of cobalt or nickel in the electrolytic bath containing $MnSO_4$ resulted in high initial discharge capacity of 670 and 395 mA h $g^{-1}$ against the undoped EMD with a discharge capacity of 220 mA h $g^{-1}$ in a Zn-$MnO_2$ system using KOH electrolyte. The obtained value is significantly higher than the previous reported values for aqueous Zn-$MnO_2$ rechargeable system [33, 42-44, 54-57]. Importantly, our current work explores in-situ doping of bivalent cations through electrodeposition technique which strongly improve the storage capacity of $MnO_2$ material. The beneficial of our current study is the synthesis of EMD from primary or secondary Mn ores with metal ion impurities. Selective dissolution of the ore with required amount of Mn and the specific metal cations would help to improve the electrochemical activity of the synthesized $MnO_2$ from the relevant leach liquor.

Figure 9 showed the Nyquist plots of the EIS spectra for the undoped and doped fresh EMD electrodes before any electrochemical tests. An inset view (in Fig. 9) shows the difference in behaviour in the high frequency region. The solution resistance ($R_s$) and the

charge transfer resistance ($R_{ct}$) for the undoped EMD were found to be 14 and 8 Ω. NiEMD and CoEMD electrodes showed comparatively lower solution resistance values of 6 and 2 Ω respectively than the undoped sample. Almost the same high frequency intercepts were observed for lower and higher concentrations of Ni and Co doped EMD illustrating that they had the same ionic resistance. The quasi semicircle of Rct value (7.6 Ω) seen for the doped CoEMD2 in the high frequency region is attributed to the charge transfer through the electrode/electrolyte interface [58]. The decreased resistance and inclined line seen in the low frequency corresponding to the solid state diffusion (Warburg impedance) indicates that doped EMD samples have improved electrochemical characteristics implying a better storage capability [58-59]. The decreased resistance might be attributed to the hierarchical nanostructure in the presence of NiO and $Co_3O_4$ spheres as composites in $MnO_2$ thorns. The poor cyclability of undoped EMD with continuous charge discharge cycling (Fig. 7) was due to high impedance value corresponds to high resistance as well as diffusion limitation behaviour of the material. However presence of cobalt decreased the impedance of the material suggesting more conductive behaviour of CoEMD followed by NiEMD samples.

EIS analyses of the undoped and doped samples carried out after the 1, 3, 5 and 10 charge-discharge cycles were compared in Fig. 10. After the first cycle, the solution resistance ($R_s$) and the charge transfer resistance ($R_{ct}$) were found to be 11.4 and 22.5 Ω for the undoped EMD while for the doped EMD the values are 7.2 and 10.3 Ω respectively. All the materials showed similar behaviour with marginal differences in resistance value after their 3$^{rd}$ and 5$^{th}$ cycle in comparison to that of the EIS after 1$^{st}$ cycle, implying the material is reversible and stable for initial cycles. However, after 10$^{th}$ cycle undoped EMD showed very high resistance of Rct value 40 Ω in comparison to the doped samples which is 15 Ω for CoEMD2. This shows the disproportionation of the $Mn^{3+}$ ions in the aqueous solution lead to the lower utilization of the active material upon continuous cycling. In the case of bivalent

dopants, the presence of Ni or Co acts as pillaring effect to the $MnO_2$ structure that delayed the disproportionation reaction to occur. An equivalent circuit model is proposed for a single electron transfer reaction that involves diffusion. The components in the circuit include, Cdl represents the double layer capacitance; Rs the solution resistance; Rct the charge transfer resistance and W the diffusion behavior represented by Warburg impedance. The decrease of Rct values for doped electrodes have corresponded to more current at the same voltage for CV measurements (in Fig. 8) implying the doped material can sustain higher voltage compared to undoped electrodes. After the electrochemical testing, all the electrodes displayed comparable Rs values implying the solution resistance attributed to electrolyte/electrode interface is quite similar. The Cdl value is proportional to the surface area with the establishment of a double layer having 0.0521 F $cm^{-2}$. The Warburg factor, an indication of proton diffusion rate into EMD lattice is calculated to be 0.65 Ω $cm^2$ $s^{-1/2}$.

## 4. Conclusions

The role of in-situ doping of nickel and cobalt were investigated on the structure and electrochemical activity of EMD deposited from manganese sulphate in sulphuric acid bath through a facile galvanostatic electrodeposition method. Optimal amount of dopant in the EMD plays a key role in improving the energy storage. The important outcomes of the present work are summarised below:

- The presence of NiO, CoO and $Co_3O_4$ in the EMD composite enhances the storage capability of the Zn-$MnO_2$ battery.
- In-situ doping of transition metal ions Ni and Co strongly affects the nucleation and growth of the EMD resulting in sea-urchin and cauliflower like hierarchical nanostructures. The presence of mesopores increases with an increase in pore size for the doped EMD materials.

- EMD doped with about 2 % by weight of Co and about 1% by weight of Ni showed highest storage capacity of 670 and 395 mA h $g^{-1}$ respectively in comparison to the undoped EMD having a meagre amount of 220 mA h $g^{-1}$.
- All the doped EMD samples showed better cycleability than the undoped EMD. However EMD doped with 0.5% of Ni showed the best cycle life stability among all followed by the EMDs with 1 % Ni (NiEMD2) and 2 % Co (CoEMD2). The optimum content of dopant is identified to be between 0.5 % and 1 % Ni in EMD.

**Acknowledgements**

This research was supported under ARC's Discovery Projects funding scheme (DP1092543). The views expressed herein are those of the authors and are not necessarily those of the Australian Research Council. The authors would like to acknowledge AINSE Research Grant (ALNGRA15545) to carry out the microscopy work at ANSTO. Authors are thankful to Ajit Dash for providing the TEM access at CSIR-IMMT.

**References**

1. P. Poizot, S. Laruelle, S. Dupont and J. M. Tarascon, *Nature* **2000**, *407*, 496.
2. S. Grugeon, S. Laruelle, R. Herrera-Urbina, L. Dupont, P. Poizot and J. M. Trarscon, *J. Electrochem. Soc.* **2001**, *148*, A285.
3. P. Poizot, S. Laruelle, S. Grugeon and J. M. Tarascon, *J. Electrochem. Soc.* **2002**, *149***,** A1212.
4. X. H. Huang, J. P. Tu, X. H. Xia, X. L. Wang, J. Y. Xiang, L. Zhang and Y. Zhou, *J. Power Sources* **2009**, *188*, 588.
5. X. H. Huang, C. B. Wang, S. Y. Zhang and F. Zhou, *Electrochim. Acta* **2011**, *56*, 6752.
6. X. H. Huang, J. P. Tu, X. H. Xia, X. L. Wang and J. Y. Xiang, *Electrochem. Commun.* **2008**, *10*, 1288.
7. Y. Sun, X. Hu, W. Luo and Y. Huang, *J. Mater. Chem.* **2012**, *22*, 13826.
8. Y. He, L. Huang, J. S. Cai, X. M. Zheng and S. G. Sun, *Electrochim. Acta* **2010**, *55*, 1140.
9. W.-Y. Li, L.-N. Xu and J. Chen. Adv. Funct. Mater. **2005**, *15*, 851.
10. J. Zhu, Y.K. Sharma, Z. Zeng, X. Zhang, M. Srinivasan, S. Mhaisalkar, H. Zhang, H. H. Hng and Q. Yan, *J. Phys. Chem. C* **2011**, *115*, 8400.
11. M. V. Reddy, G. Prithvi, K.P. Loh and B.V.R. Chowdari, *ACS Appl. Mater. Interfaces* **2014**, *6*, 680.
12. X.H. Huang, J.P. Tu, B. Zhang, C.Q. Zhang, Y. Li, Y.F. Yuan and H.M. Wu, *J. Power Sources* **2006**, *161*, 541.

13. Yu. Yao, J. Zhang, Z. Wei and A. Yu, Int. *J. Electrochem. Sci*. **2012**, *7*, 1433.
14. A. Urfer, G.A. Lawrance and D.A.J. Swinkels, *J. Appl. Electrochem*. **1997**, *27*, 667.
15. K.V. Kordesch and M. Dekker, (**1974**) Batteries. Dekker, New York
16. K.V. Kordesch and M. Weissenbacher, *J. Power Sources* **1994**, *51*, 61.
17. E. Machefaux, L.I. Hill and D. Guyomard, The Electrochemical Society, 204th Meeting, **2003**, Abstract # 365.
18. W. Jantscher, L. Binder, D.A. Fiedler, R. Andreaus and K. Kordesch, *J. Power Sources* **1999**, *79*, 9.
19. S. Chou, F. Cheng and J. Chen, *J. Power Sources* **2006**, *162*, 727.
20. M. Nakayama, A. Tanaka, Y. Sato, T. Tonosaki and Kotaro Ogura, *Langmuir* **2005**, *21*, 5907.
21. K. Rajendra Prasad and N. Miura, *Electrochem. Commun.* **2004**, *6*, 1004.
22. Y. S. Chen and C. C. Hu, *Electrochem. Solid-State Lett.* **2003**, *6*, A210.
23. P.Y. Chuang, C.C.Hu, *Mater. Chem and Phys.* **2005**, *92*, 138.
24. J. K. Chang, M. T. Lee, C. H. Huang, W.T. Tsai, *Mater. Chem. and Phys.* **2008**, *108*, 124.
25. H. M. Lee, K. Lee and C.K. Kim, *Mater.* **2014**, *7*, 265.
26. T. Nguyen, M. Boudard, L. Rapenne, M. J. Carmezim and M. F. Montemor, *J. Mater. Chem. A* **2015**, *3*, 10875.
27. H. Kim and B. N. Popov, *J. Electrochem. Soc.* **2003**, *150*, D56.
28. C. H. Lu and H. C. Wang, *J. Euro. Ceramic Soc.* **2003**, *23*, 865.
29. B. C. Kim, C. J. Raj, W. J Cho, W.G. Lee, H. T. Jeong, K. H. Yu, *J. Alloys Compd.* **2014**, *617*, 491.
30. Y. J. Li, H. Xu, L. Kong, H.C. Li, C.X. Li, X. Z. Zhang and Q. Han, *J. Inorg. Mater.* **2014**, *29*, 661.
31. Y.-G. Guo, J.-S. Hu and L. -J. Wan, *Adv. Mater*. **2008**, *20*, 2878.
32. S. Yin, Y. Zhang, J. Kong, C. Zou, C. Ming, X. Lu, J. Ma, F. Y. C. Boey and X. Chen, *ACS Nano* **2011**, *5*, 3831.
33. A. Biswal, B.C. Tripathy, T. Subbaiah, D. Meyrick and M. Minakshi, *J. Solid State Electrochem.* **2013**, *17*, 1349.
34. C. Xu, X. Wang, J. Zhu, X. Yang and L. Lu, *J. Materials Chem.* **2008**, *18*, 5625.
35. F. C. Walsh, C. Ponce de Leon, D. V. Bavykin, C. T. J. Low, S. C. Wang, C. Larson, *Trans. Institute of Mater. Finishing* **2015**, *93*, 229.
36. F. C. Walsh, C. Ponce de Leon, D. V. Bavykin, C. T. J. Low, S. C. Wang, C. Larson, *Trans. Institute of Mater. Finishing* **2015**, *93*, 241.
37. A. Kozawa, *Prog. Batt. Solar Cells* **1998**,*7*, 327.
38. H. Tamura, M. Nagayama and R. Furuichi, *J. Electrochem. Soc*. **1994**, *141*, 2035.
39. K. C. Liu and M. A. Anderson, *J. Electrochem. Soc*. 1996, *143*, 124.
40. V. Gupta, T. Kusahara, H. Toyama, S. Gupta and N. Miura, *Electrochem. Commun.* **2007**, *9*, 2315.
41. X. Xia, J. Tu, X. Wang, C. Gu and X. Zhao, *J. Mater. Chem*. **2011**, *21*, 671.
42. G. Girish Kumar and S. Sampath, *J. Electrochem. Soc*. **2003**, *150*, A608.
43. B. Hertzbeg, L. Sviridov, E. A. Stach, T. Gupta and D. Steingart, *J. Electrochem. Soc.* **2014**, *161*, A835.
44. N. D. Ingale, J. W. Gallaway, M. Nyce, A. Couzis and S. Banerjee, *J. Power Sources* **2015**, *276*, 7.
45. Y. G. Wang and Y. Y. Xia, *Electrochim. Acta* **2006**, *51*, 3223.
46. H. Li, Y. Li, R. Wang and R. Cao, *J. Alloys Compd*. **2009**, *481*, 100.
47. U. M. Patil, R. R. Salunkhe, K. V. Gurav and C. D. Lokhande, *Appl. Surf. Sci*. **2008**, *255*, 2603.
48. M. Minakshi and D. Meyrick, *Electrochim. Acta* **2013**, *101*, 66.

49. L. Wang, B. Liu, S. Ran, H. Huang, X. Wang, B. Liang, D. Chen and G. Shen, *J. Mater. Chem*. **2012**, *22*, 23541.
50. Y. G. Li, B. Tan and Y. Y. Wu, *Nano Lett*. **2008**, *8*, 265.
51. F. M. Zhan, B. Y. Geng and Y. J. Guo, *Chem.–Eur. J*. **2009**, *15*, 6169.
52. E. Bertel and N. Memmel, *Appl. Phys. A* **1996**, *63*, 523.
53. N. Li, C. J. Patrissi, G. Che and C. R. Martin, *J. Electrochem. Soc.* **2000**, *147*, 2044
54. A. Biswal, B.C. Tripathy, T.Subbaiah, D. Meyrick, M. Ionescu and M. Minakshi, *Metall. Mater. Trans. E* **2014**, *1*, 226.
55. V. Raghuveer and A. Manthiram, *J. Power Sources* **2006**, *159*, 1468.
56. V. Raghuveer and A. Manthiram, *J. Power Sources* **2006**, *163*, 598.
57. D. K. Walanda, G. A. Lawrance and S. W. Donne, *J. Power Sources* **2005**, *139*, 325.
58. H. Song, L. Shen and C. Wang, *J. Mater. Chem. A* **2014**, *2*, 20597.
59. R. Ramkumar and M. Minakshi, *Dalton Trans.* **2015**, *44*, 6158.

**Table 1** Electrolyte composition of the different EMDs

| **Electrolyte composition (g $dm^{-3}$)*** | **Symbolic representation of the synthesized EMD** |
|---|---|
| 60Mn | EMD |
| 45 Mn +15 Ni | NiEMD1 |
| 30 Mn +30 Ni | NiEMD2 |
| 45 Mn + 15 Co | CoEMD1 |
| 30 Co + 30 Co | CoEMD2 |
| 20 Mn + 20 Ni + 20 Co | CoNiEMD |

*Sulphuric acid concentration in each case was with 1:2 ratio of [Mn] of manganese sulphate

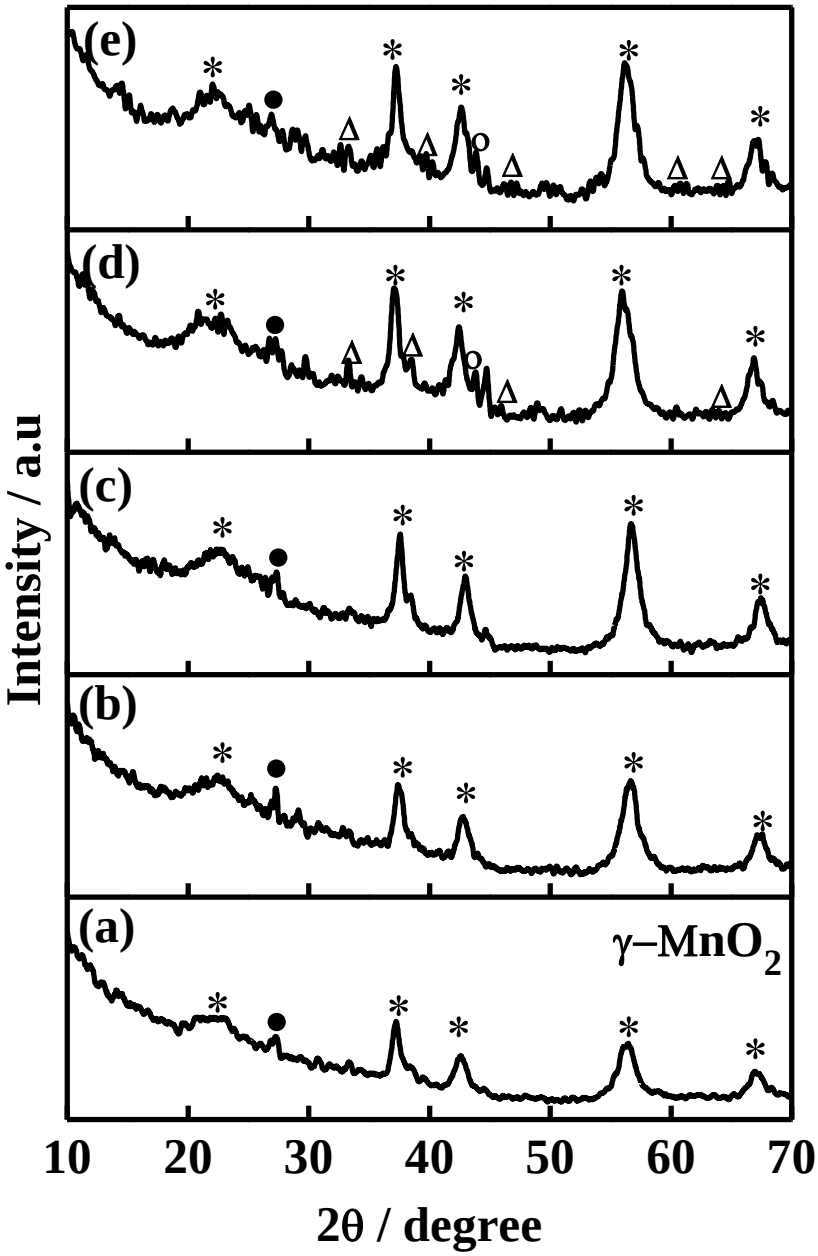


**Figure 1** X-ray diffraction pattern of (a) EMD (undoped), (b) NiEMD1, (c) NiEMD2, (d) CoEMD1, and (e) CoEMD2 (*: $MnO_2$, •: unknown phase, Δ: $Co_3O_4$, o: CoO, ).

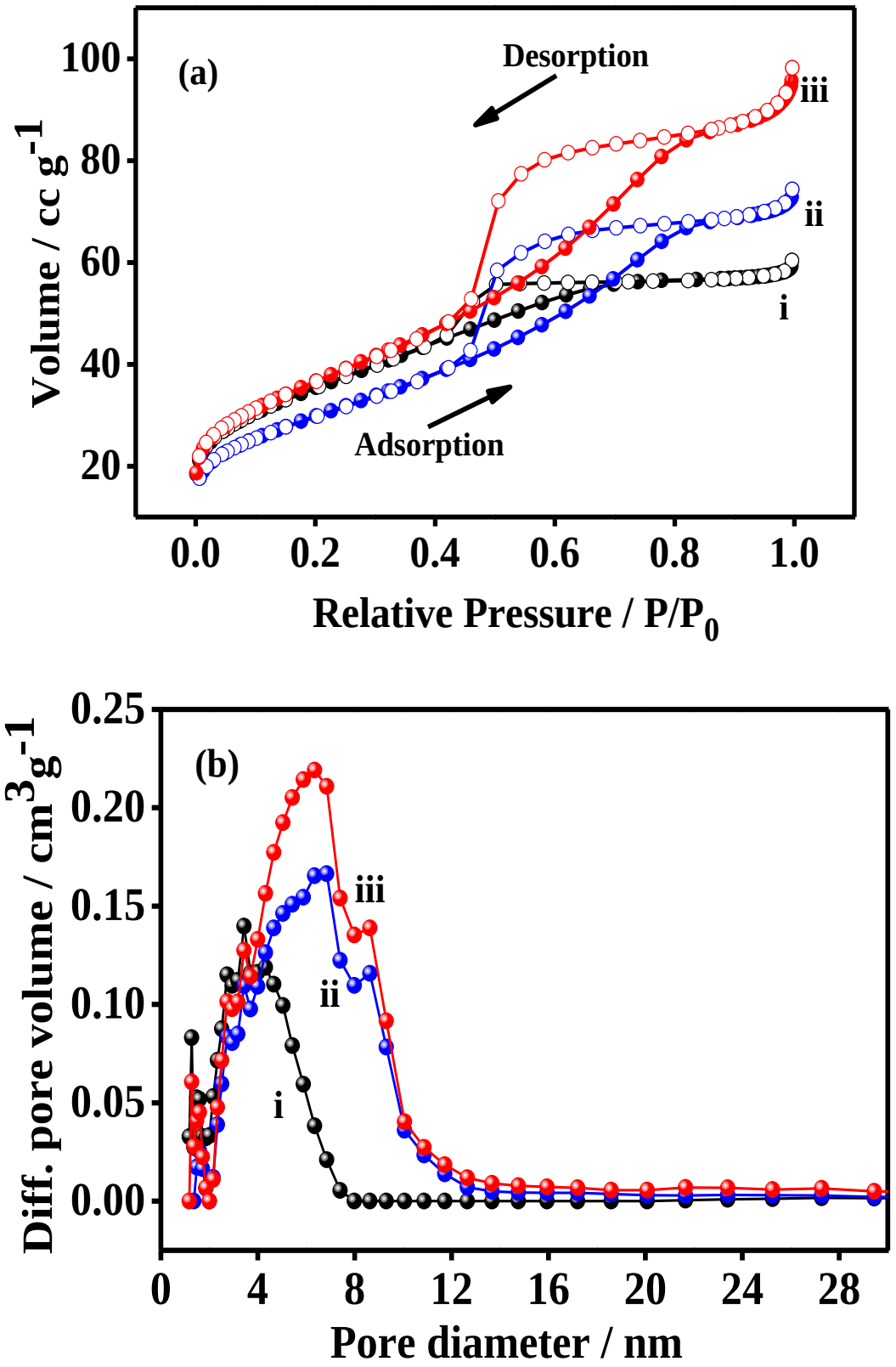


**Figure 2** (a) Nitrogen adsorption-desorption and (b) pore size distribution plots of (i) EMD, (ii) NiEMD2, and (iii) CoEMD2 composites.

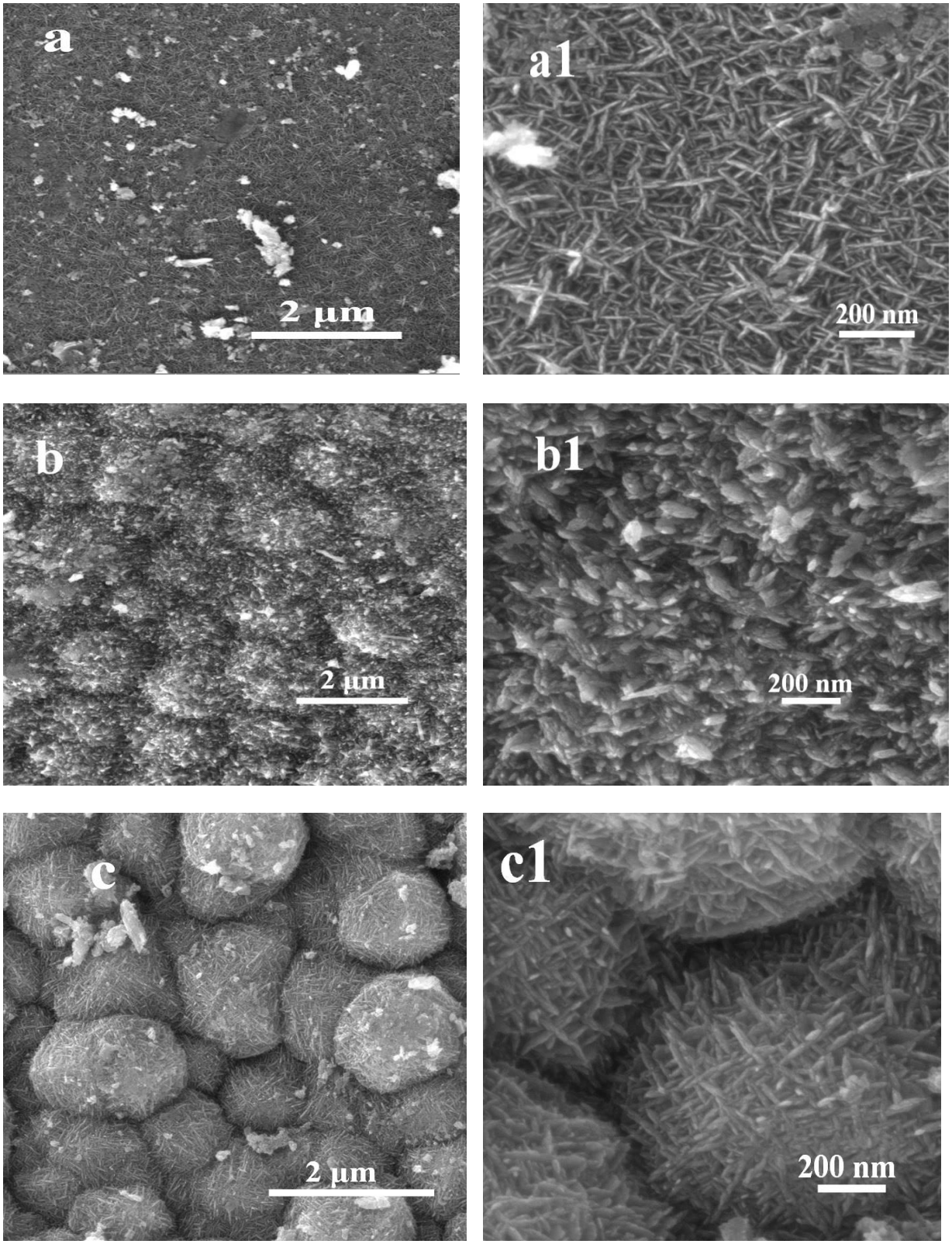


**Figure 3** FIBSEM images of (a) EMD, (b) NiEMD1, and (c) NiEMD2 with a low magnification. The respective high magnification images are shown in a1, b1 and c1. Sea-urchin like morphology is seen in fig. 3 c1.

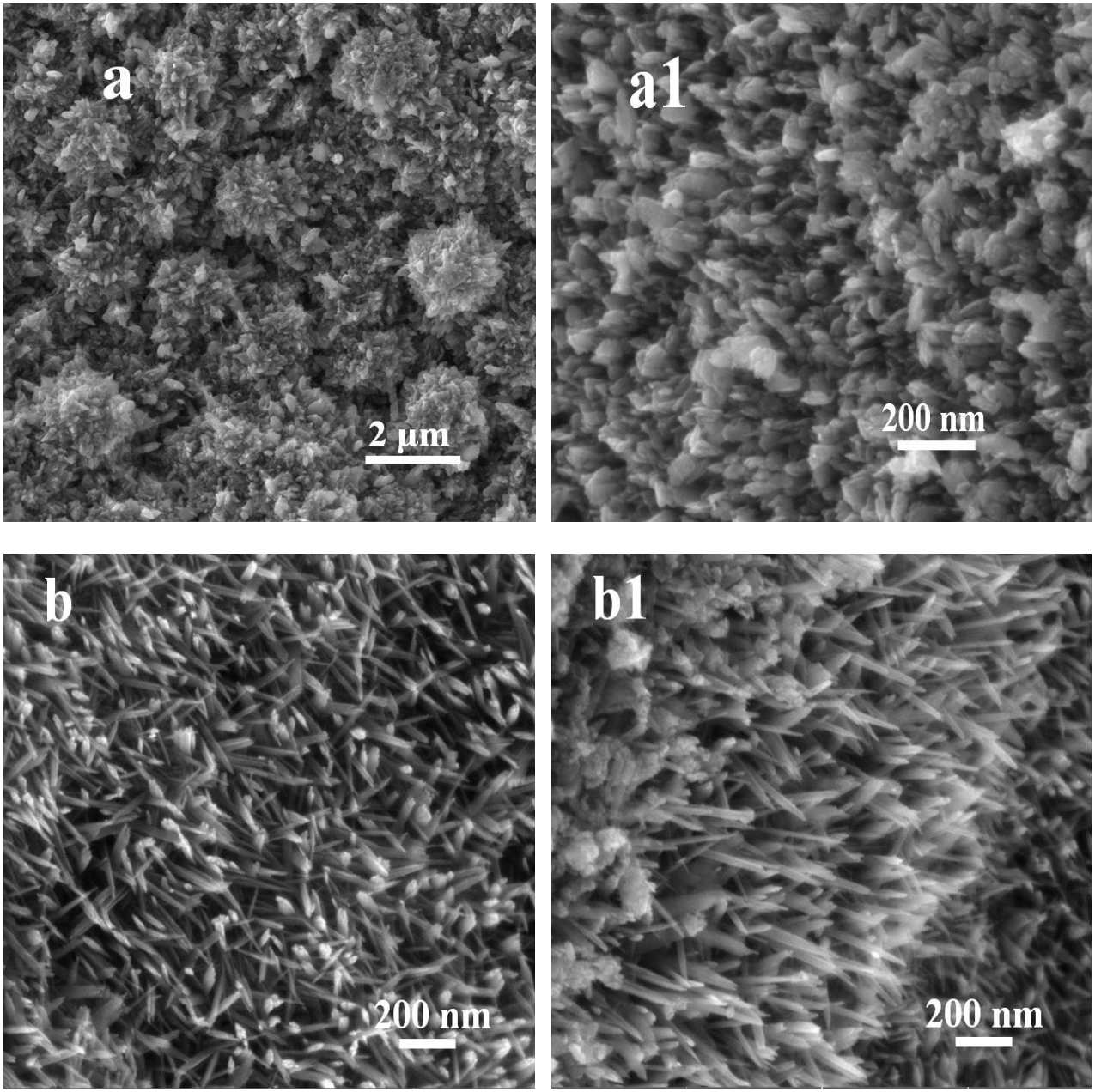


**Figure 4** FIBSEM images of CoEMD1 with (a) low and (a1) high magnifications. Cross-sectional images of CoEMD1 at different locations are shown in (b) and (b1) under the same magnifications. Cauliflower crystallites having uniform flower bud shaped nano grains are seen.

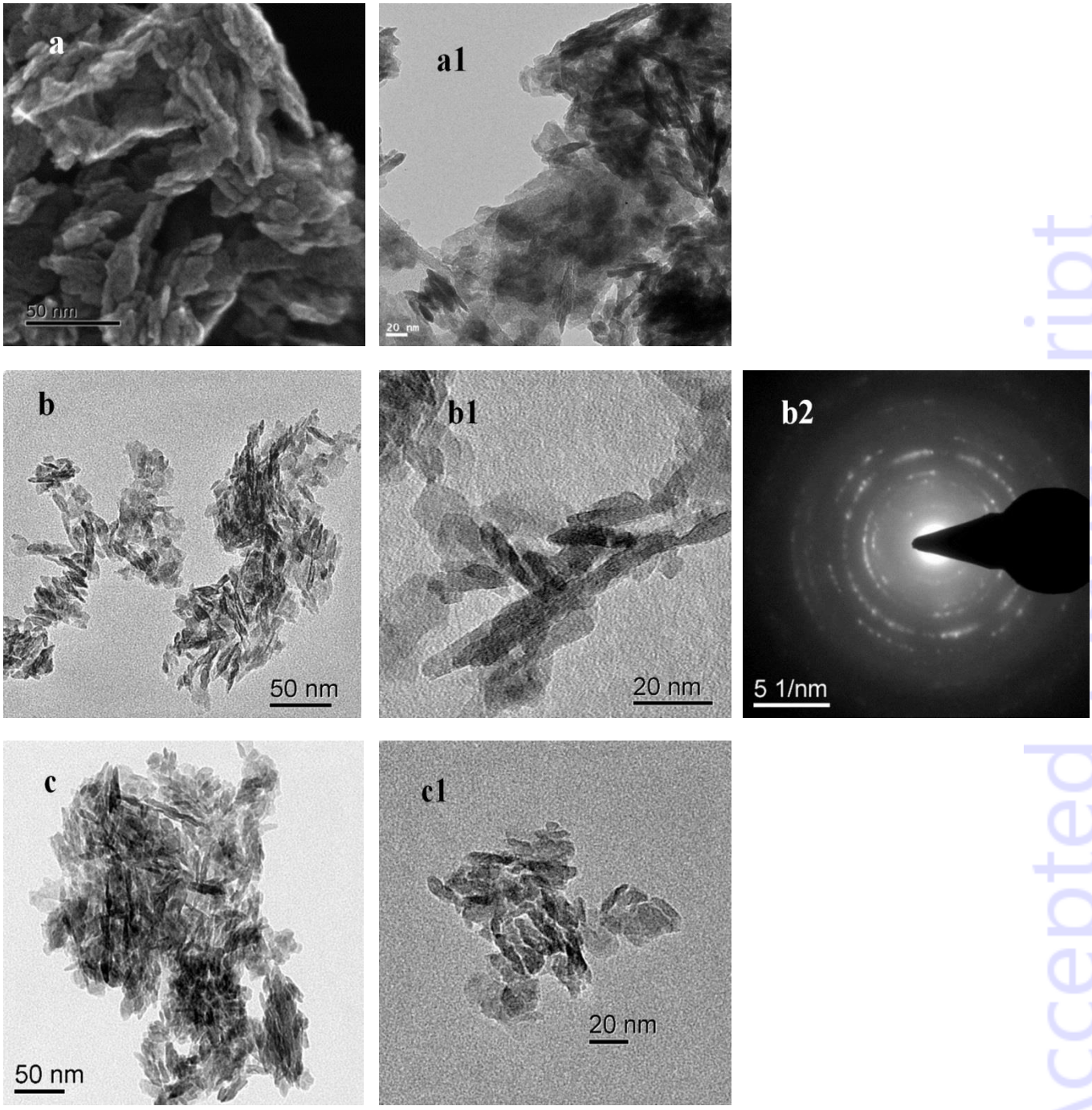


**Figure 5** TEM images of the (a) EMD, (b) NiEMD2, and (c) CoEMD2 with a low magnification. The respective high magnification images are shown in a1, b1 and c1. The selected electron area diffraction pattern for NiEMD2 is shown in b2.

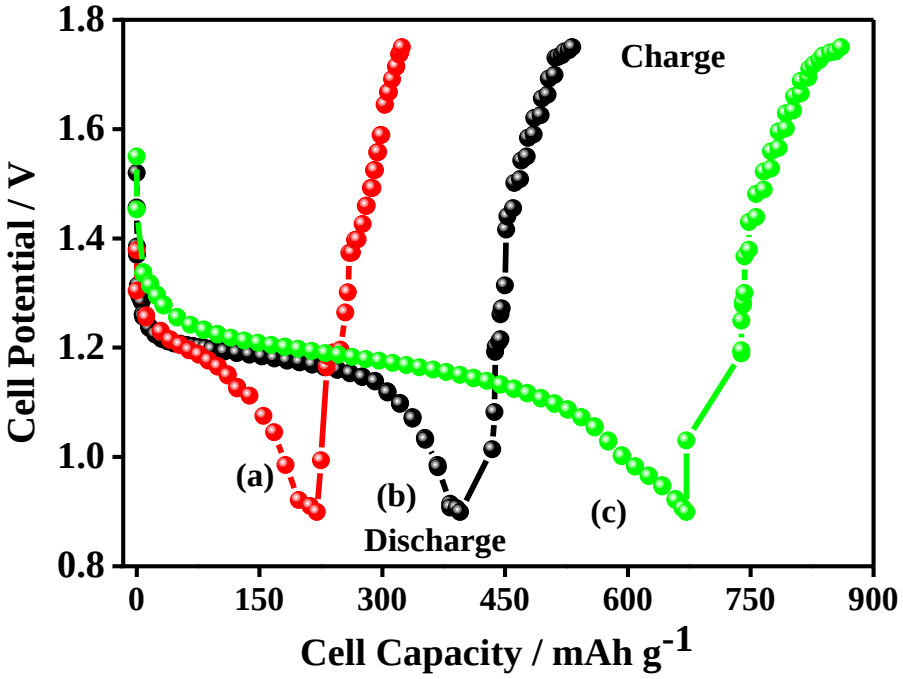


**Figure 6** The first discharge-charge profile of (a) undoped and doped (b) NiEMD2 and (c) CoEMD2 as cathode in Zn - EMD cell using 9M KOH discharged (2 mA) and charged (4 mA) at different current rates.

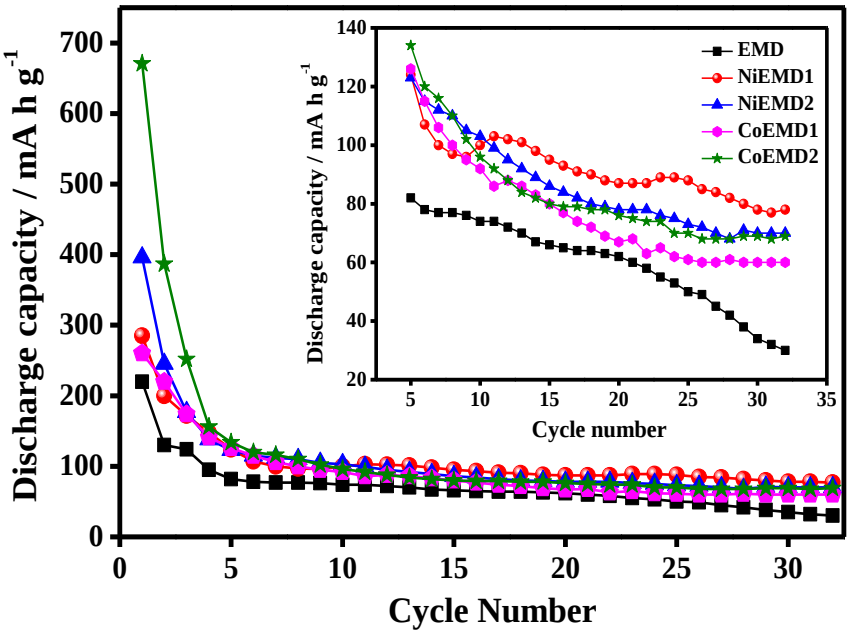


**Figure 7** Galvanostatic discharge capacity versus cycling behaviour of undoped and doped EMD cathode vs. Zn cells.

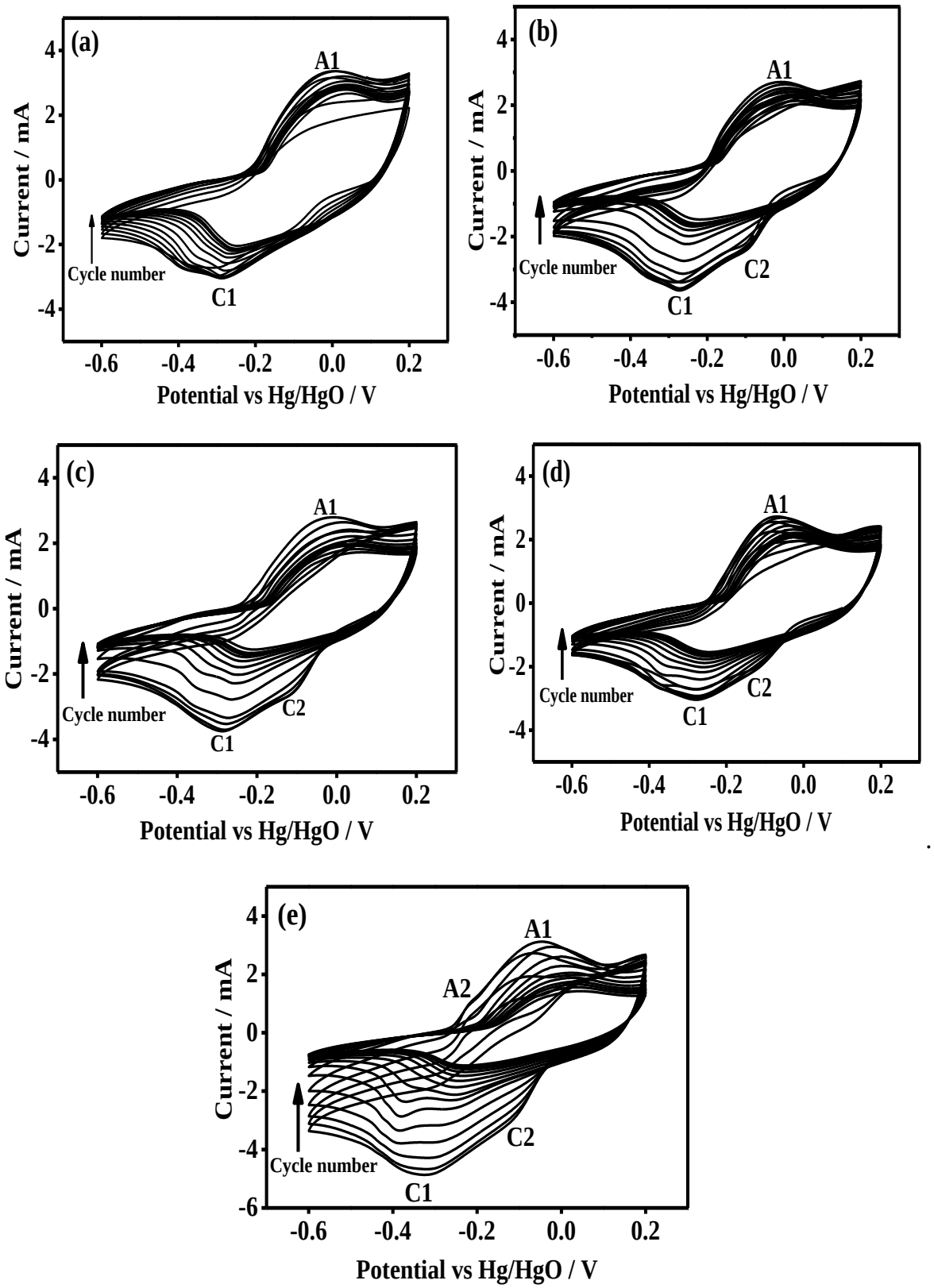


**Figure 8** Cyclic voltammetry (CV) plots of (a) EMD, (b) NiEMD1, (c) NiEMD2, (d) CoEMD1, and (e) CoEMD2 at a scan rate of 0.15mV $s^{-1}$. The term "C" and "A" denotes reduction (cathodic) and oxidation (anodic) peaks respectively. All the materials have been cycled for 30 cycles.

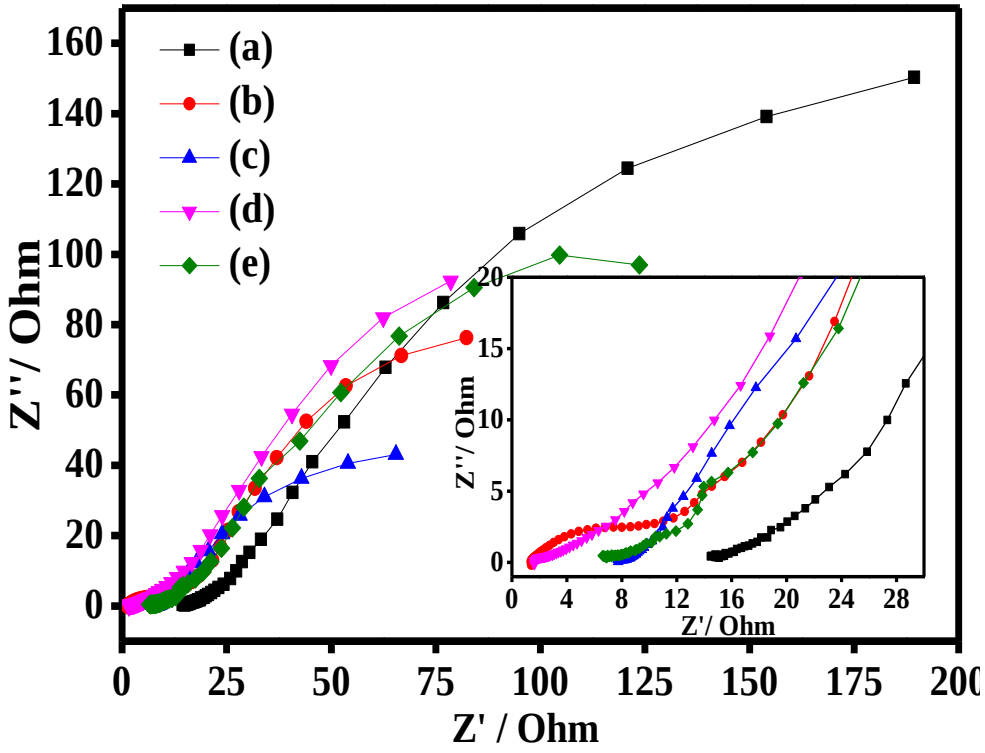


**Figure 9** Electrochemical impedance spectroscopy (EIS) plots of as-electrodeposited (a) EMD, (b) NiEMD1, (c) NiEMD2, (d) CoEMD1, (e) CoEMD2 samples.

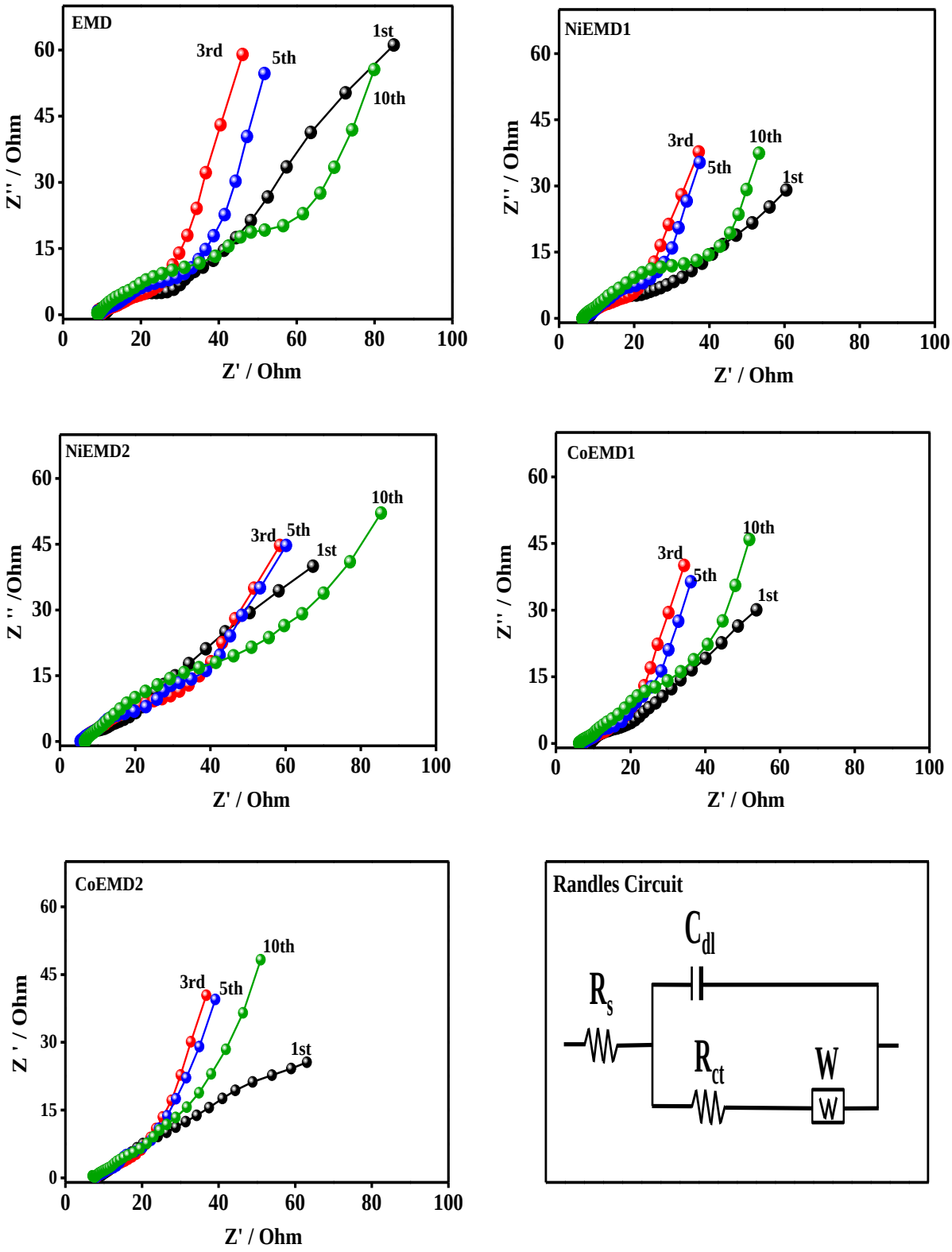


**Figure 10** Electrochemical impedance spectroscopy (EIS) plots of undoped and doped EMD samples after 1st, 3rd, 5th and 10th charge-discharge cycles. A possible equivalent circuit has been proposed.

**Electronic supplementary information**

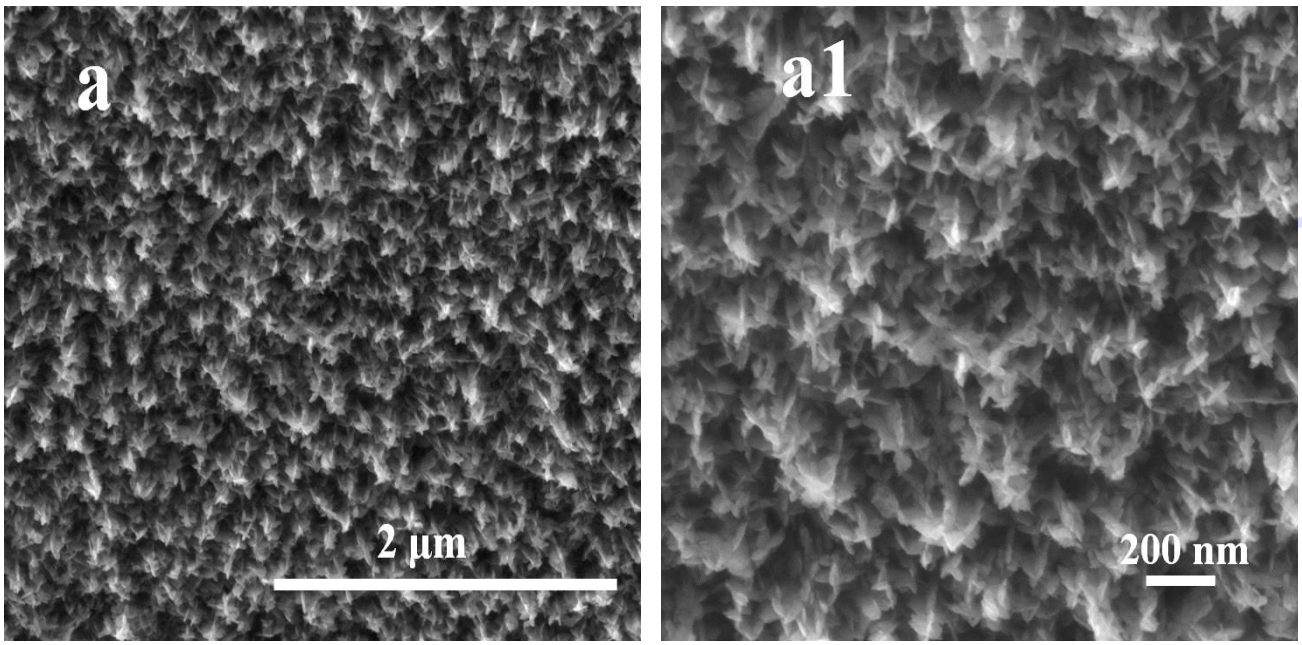


**Figure S1** FIBSEM images of CoEMD2 with (a) low and (a1) high magnifications. Star shaped nano grains having pyramidal alignment are seen.

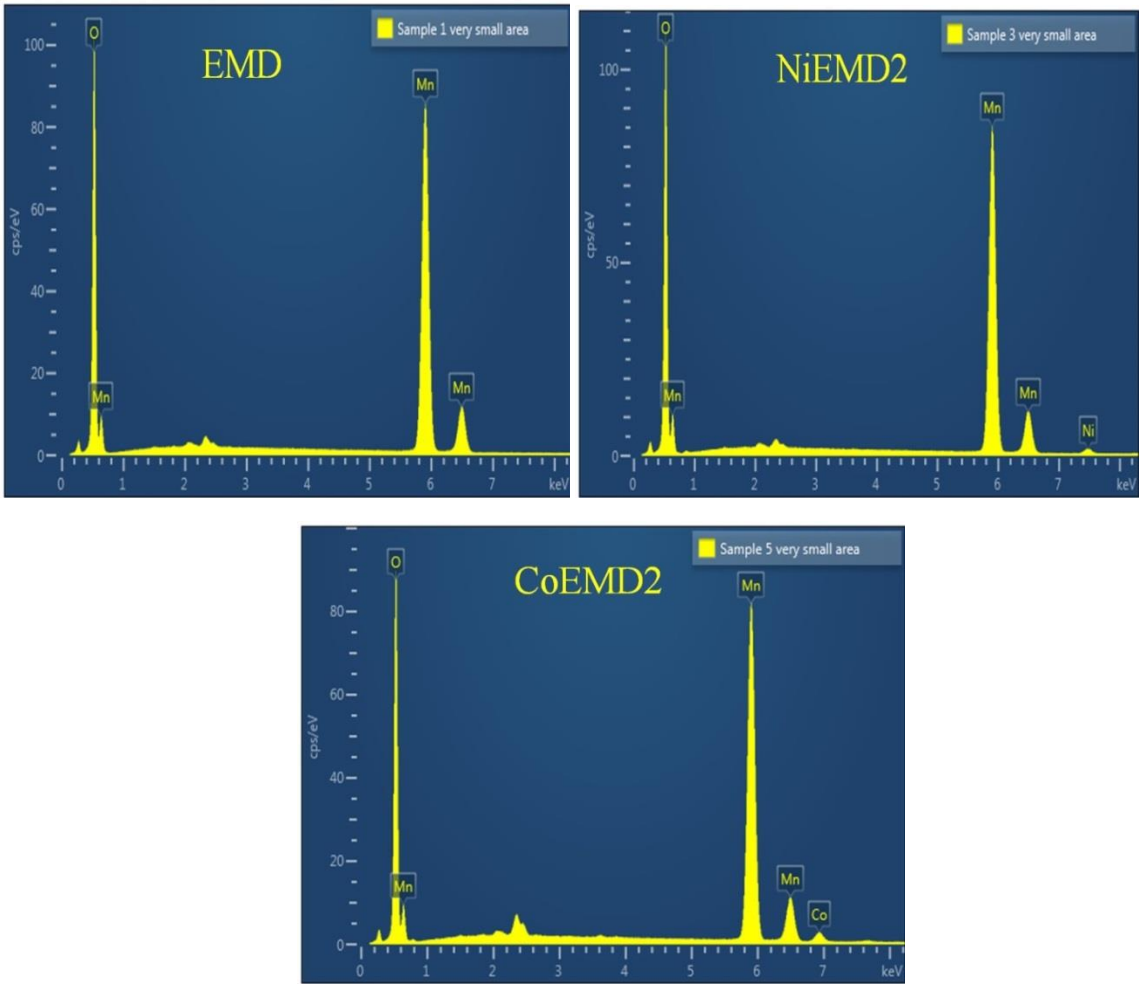


**Figure S2** Energy Dispersive X-ray spectra (EDS) of the EMD (undoped) and NiEMD2 and CoEMD2. The spectra showed the presence of Ni and Co in the EMD composite which is conformed quantitatively from inductive coupled plasma (ICP) analysis to be 1 % and 2% respectively.

**Role of both Ni and Co dopants in EMD (CoNiEMD)**

Figure (S3) shows the CV plot of the CoNiEMD samples deposited from a bath containing equal concentration of Ni, Co and Mn as sulphate precursors (see table 2). The CV plot of the CoNiEMD sample exhibits three reduction peaks (C1, C2 and C3) and subsequent two oxidation peaks (A1 and A2) during the cathodic and anodic scan, respectively. Reduction peaks at -0.41 (C1); -0.29 (C2) and -0.08V (C3) correspond to the reduction of nickel[1-3],

cobalt[4-6] and manganese[7-8] cations respectively. However, it is been observed from the CV plot that only Co (A2) and Mn (A1) are reversible[9]. It is also observed that in presence of two different dopants (both Co and Ni), the reduction peak for Mn (C1) shifted towards more negative potential of -0.41 V which maximises the peak separation (0.6 V) to that of the other individual dopants studied (see Fig. 9 in the main article). The corresponding discharge capacity vs. cycle life plot for CoNiEMD showed (in Figure S4) an initial discharge capacity of 253 mA h $g^{-1}$ which is the lowest among all the doped samples studied, however it showed an average capacity of 64 mA h $g^{-1}$ after 30$^{th}$ cycle which is slightly higher than the CoEMD1 (60 mA h $g^{-1}$) but lower than the other doped samples. Figure S5 shows the TEM imaging of CoNiEMD exhibiting the contrast in regions with an individual grain size of about 20 nm in length and 10 nm in diameter of each grain. The contrast in the region corresponds to the dopants present in the EMD structure. The high resolution TEM of this region shows the particles are clustered together that could inhibit the ionic transport and the lattice strain contrasts implies the dislocations/defects in the CoNiEMD structure.

In concern to the synthesis condition, during the electrodeposition of EMD from a mixed bath containing 20 g $dm^{-3}$ Co, 20 g $dm^{-3}$ Ni and 20 g $dm^{-3}$ Mn, the current efficiency decreased significantly due to lower concentration of Mn than the required level of 30 g $dm^{-3}$. Therefore, the sample with the composition of CoNiEMD (1:1:1) is found to be not suitable for electrode in a battery system. The observed performance could be that the host $MnO_2$ is not able to accommodate both bivalent cations at the given ratio. To the best of our knowledge, there is no literature is available on having all cations in the same ratio in $MnO_2$ structure and therefore, it is hard to draw more insights into it.

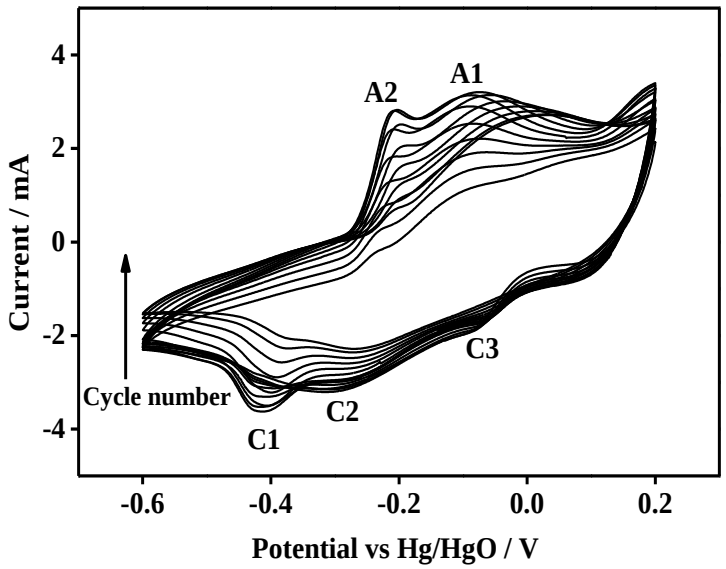


**Figure S3** Cyclic voltammetry (CV) plots of CoNiEMD at a scan rate of 0.15mV $s^{-1}$. The term "C" and "A" denotes reduction (cathodic) and oxidation (anodic) peaks respectively. All the materials have been cycled for 30 cycles.

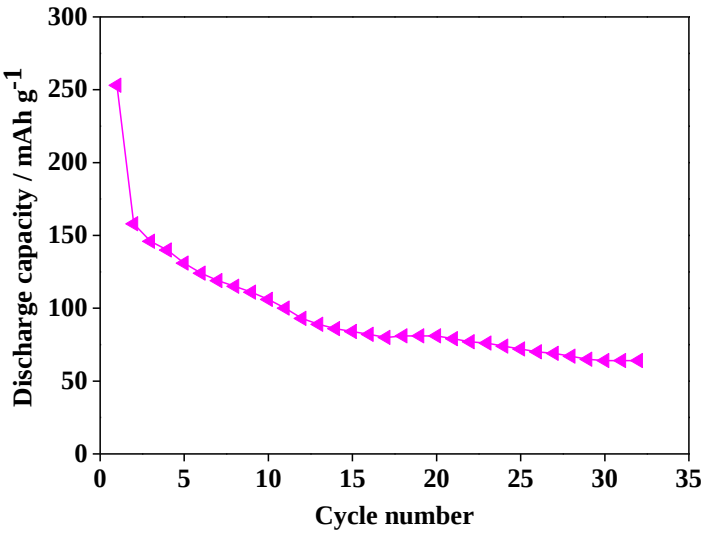


**Figure S4** Galvanostatic discharge capacity versus cycling behaviour of CoNiEMD cathode vs. Zn cells.

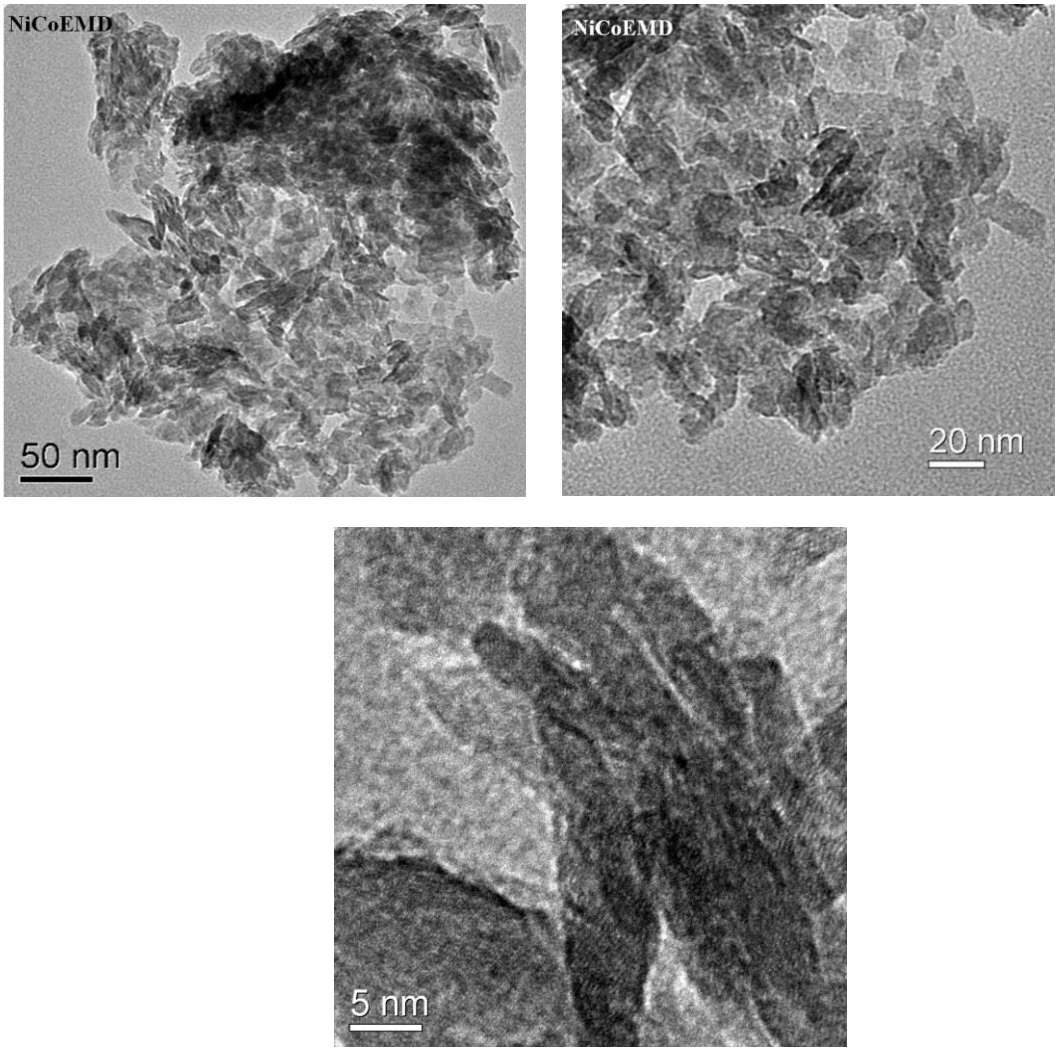


**Figure S5** TEM images of the doped CoNiEMD powder under different magnifications.

## References


1. Y. G. Wang and Y. Y. Xia, *Electrochim. Acta*, **2006**, *51*, 3223.
2. H. Li, Y. Li, R. Wang and R. Cao, *J. Alloys Compd*., **2009**, *481*, 100.
3. U. M. Patil, R. R. Salunkhe, K. V. Gurav and C. D. Lokhande, *Appl. Surf. Sci*., **2008**, *255*, 2603.
4. L. Wang, B. Liu, S. Ran, H. Huang, X. Wang, B. Liang, D. Chen and G. Shen, *J. Mater. Chem*., **2012**, *22*, 23541.
5. Y. G. Li, B. Tan and Y. Y. Wu, *Nano Lett*., **2008**, *8*, 265.
6. F. M. Zhan, B. Y. Geng and Y. J. Guo, *Chem.–Eur. J*., **2009**, *15*, 6169.
7. M. Minakshi and D. Meyrick, *Electrochim. Acta*, **2013**, *101*, 66.
8. A. Biswal, B.C. Tripathy, T.Subbaiah, D. Meyrick, M. Ionescu and M. Minakshi, *Metall. Mater. Trans. E*, **2014**, *1*, 226
9. M. Minakshi Sundaram, T. Watcharatharapong, S. Chakraborty, R. Ahuja, S. Duraisamy, P. R. Rao, and N. Munichandraiah, *Dalton Trans*. **2015**, *44*, 20108.

**TOC**

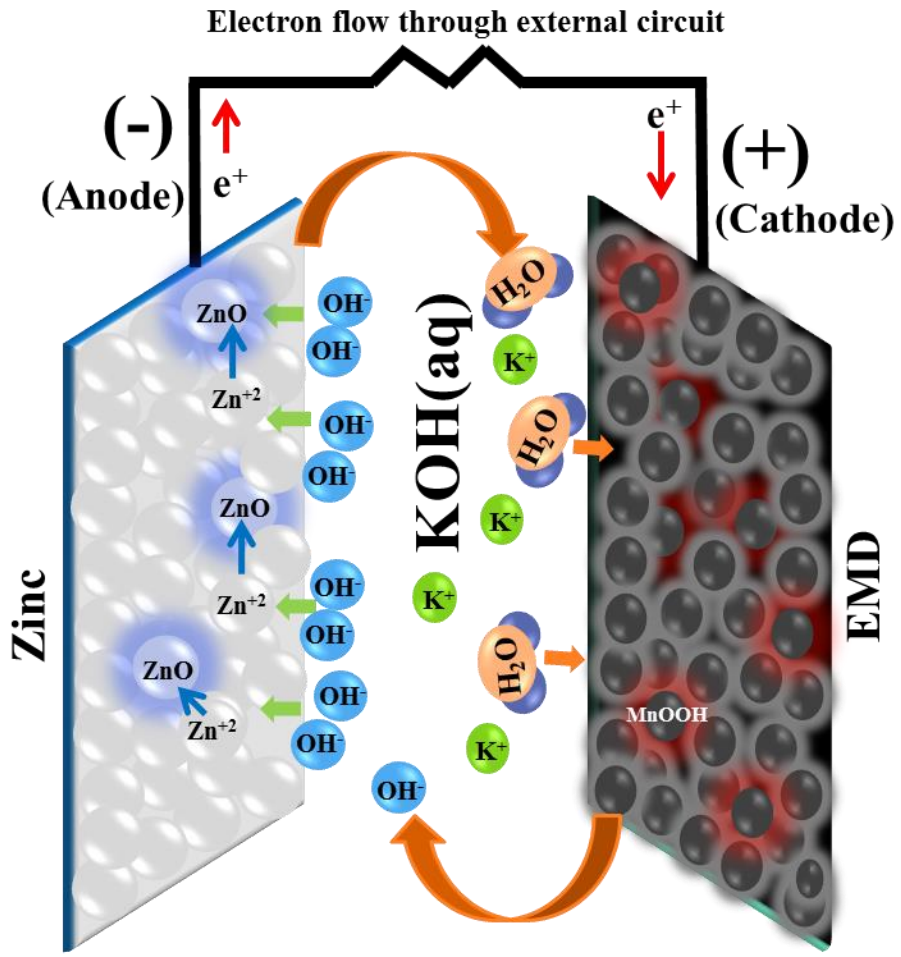


EMD is most widely used cathode material in battery industries, as it contains most electro active γ-phase. In-situ doping of nickel and cobalt in EMD material enhanced the storage capability of the Zn-$MnO_2$ secondary battery as illustrated here.